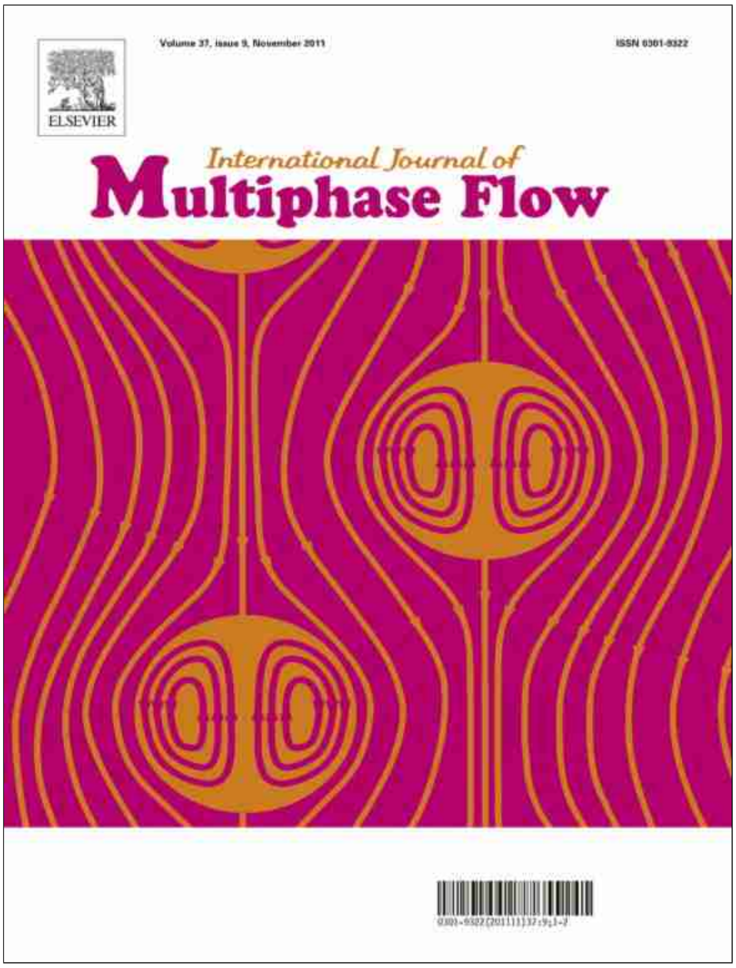
Volume 37, Issue 9, November 2011
ISSN 0301-9322
ELSEVIER
International Journal of
Multiphase Flow

International Journal of Multiphase Flow 37 (2011) 1135–1146

Contents lists available at ScienceDirect

International Journal of Multiphase Flow

journal homepage: www.elsevier.com/locate/ijmulflow

# Adiabatic and diabatic two-phase venting flow in a microchannel

Milnes P. David *, Julie E. Steinbrenner, Josef Miler, Kenneth E. Goodson

*Department of Mechanical Engineering, Stanford University, 440 Escondido Mall, Room 224, Stanford, CA 94305, USA*

ARTICLE INFO

*Article history:*
Received 22 October 2010
Received in revised form 24 June 2011
Accepted 27 June 2011
Available online 7 July 2011

*Keywords:*
Phase separation
Microchannel
Adiabatic two-phase flow
Diabatic two-phase flow
Flow regime

ABSTRACT

The growth and advection of the vapor phase in two-phase microchannel heat exchangers increase the system pressure and cause flow instabilities. One solution is to locally vent the vapor formed by capping the microchannels with a porous, hydrophobic membrane. In this paper we visualize this venting process in a single 124 μm by 98 μm copper microchannel with a 65 μm thick, 220 nm pore diameter hydrophobic Teflon membrane wall to determine the impact of varying flow conditions on the flow structures and venting process during adiabatic and diabatic operation. We characterize liquid velocities of 0.14, 0.36 and 0.65 m/s with superficial air velocities varying from 0.3 to 8 m/s. Wavy-stratified and stratified flow dominated low liquid velocities while annular type flows dominated at the higher velocities. Gas/vapor venting can be improved by increasing the venting area, increasing the trans-membrane pressure or using thinner, high permeability membranes. Diabatic experiments with mass flux velocities of 140 and 340 kg/s/m$^2$ and exit qualities up to 20% found that stratified type flows dominate at lower mass fluxes while churn-annular flow became more prevalent at the higher mass-flux and quality. The diabatic flow regimes are believed to significantly influence the pressure-drop and heat transfer coefficient in vapor venting heat exchangers.



## 1. Introduction

High performance thermal management for integrated circuits is a pressing need in the electronics industry. The 2009 and 2010 International Technology Roadmap for Semiconductors (ITRS) predicts heat fluxes of >100 W/cm$^2$ for high performance microprocessors, device temperatures less than 70 °C and overall device-to-ambient thermal resistance of less than 0.2 K/W ("2009 ITRS", 2011; "2010 ITRS Update", 2011). Thermal management of hotspots is particularly challenging because the local heat flux is substantially higher. Additionally, shrinking enclosures and 3D IC architectures (Koo et al., 2005; Bernstein et al., 2007) require cooling solutions of the same scale as the chip and which could potentially be fabricated within the chip itself.

Microfluidic liquid cooling is one of the most promising solutions for meeting these thermal, geometric and fabrication requirements. Single phase liquid cooling with microstructured heat exchangers (Qu and Mudawar, 2002; Garimella and Singhal, 2004; Kandlikar and Grande, 2004) is now a commercialized solution but requires large, high-power pumps to drive the working fluid at rates of hundreds of milliliters per minute to provide the required thermal resistance and maintain temperature uniformity. Passive two-phase microfluidic solutions such as heat pipes are unable to dissipate high heat fluxes and have thermal resistances an order higher than required (Kandlikar et al., 1999). Two-phase forced convective microfluidics are capable of dissipating the required heat flux while simultaneously maintaining a more uniform junction temperature across the device by leveraging the large enthalpy change and fixed saturation temperatures during vaporization (Jiang and Wong, 2001; Hetsroni et al., 2002).

However, vaporization and the subsequent two-phase flow leads to a large increase in pressure due to the higher friction of the vapor phase, the interaction between the phases, and the acceleration of the liquid to the vapor phase. The increase in pressure drop during adiabatic and diabatic flow is well documented in texts (Carey, 1992; Tong and Tang, 1997a) and literature. The increase in pressure drop during phase-change has been experimentally observed in our recent work in copper microchannels (David et al., 2008, accepted for publication) and by various authors such as Zhang et al. (2002), Lee and Garimella (2008) and Qu and Mudawar (2003). This increased system pressure during two-phase flow increases the required pumping power and manifests itself as an additional thermal resistance by shifting saturation conditions such that the working fluid vaporizes at a higher temperature.

The nucleation and growth of the vapor phase also result in instabilities. Wu and Cheng (2004) carried out their studies in silicon microchannels with hydraulic diameters of 186 μm and found multiple types of instabilities with maximum wall temperature oscillations of the order of hundreds of degrees celsius. Static Ledinegg instabilities due to the pressure rise during two-phase flow in parallel channel systems lead to flow maldistribution,

* Corresponding author. Tel.: +1 650 353 1284.
*E-mail address:* milnespd@us.ibm.com (M.P. David).

0301-9322/$ - see front matter 
doi:10.1016/j.ijmultiphaseflow.2011.06.013

starving boiling channels of fluid and leading to earlier dry-out; details of this instability and its impact are described in greater detail by Tong and Tang (1997b) and Zhang et al. (2009).

We have proposed and developed a cooling solution that addresses both the pressure drop and instability problem by locally venting the vapor phase (David et al., 2007, 2008). In this solution we incorporate a micro/nanoporous hydrophobic membrane on one side of the microchannels. The hydrophobicity of this membrane stops the liquid phase from leaking out of the system but allows the vapor to escape freely. 1-D flow simulations based on bulk two-phase pressure drop and heat transfer correlations predict that the pressure drop would reduce dramatically in the case of complete venting and thus also eliminate the additional thermal resistance induced by the increased two-phase system pressure. 3-D FLUENT (ANSYS Inc., USA) simulations also confirm the reduction in pressure and improvement in device temperatures by reducing dry-out during bubbly vaporization (Fang et al., 2010). One of the key drawbacks in the experimental studies of the devices presented by David et al. is the inability to visualize the venting process due to the opacity of the high temperature hydrophobic Teflon membrane used. Without this information, we cannot intelligently troubleshoot the device or optimize the flow conditions and channel geometries to maximize phase separation. Knowledge of the flow regime is also critical in developing appropriate pressure drop and heat transfer models for vapor venting devices.

Two recent works in air venting/breathing visualization was carried out by Meng et al. (2007) and Alexander and Wang (2009). The work of Meng et al. (2007) focuses on the venting of gas bubbles from water and methanol solutions at room temperatures with top-down visualization carried out through transparent, polypropylene membranes. Air is introduced into the venting structure upstream and vented through the polypropylene membrane at trans-membrane pressures of 3.4–13.8 kPa. The air slugs were found to shrink in size as they traveled through the channel due to venting; a bubble evolution model was developed to describe this phenomenon. Alexander and Wang (2009) carried out side-visualization of air venting from an air–water mixture in a microfabricated silicon device with the pores directly fabricated into the channel side wall. The micron scale pores were surface-treated to provide hydrophobicity. They carried out visualization of air–water mixtures at water inlet velocities ranging between 0.5 and 3.8 cm/s and pressures up to 8 kPa and observed air removal rates up to 50 μl/min. They determined that air removal rate increases with the ratio of the pressure drop across the breather pores to the pressure drop across the bubble and that this ratio increases with channel aspect ratio and decreases with liquid flow velocity.

In this paper we discuss the development and testing of a copper visualization device that allows for side-visualization of the air–water and vapor–water flow structures while using commercially available hydrophobic, nanoporous membranes. This visualization device overcomes the need to have transparent and semi-transparent membranes or the need to microfabricate them directly into the structure. Visualization of both adiabatic and diabatic two-phase flows help develop a better understanding of gas and vapor venting from microchannels. The advantage of adiabatic experiments is the ability to accurately control the inlet quality and measure the gas venting rate while avoiding the complexities introduced by evaporation and membrane condensation to the venting process. This allowed us to carry out a more detailed analysis of the factors affecting venting rate and help generate design guidelines for gas and vapor venting devices. The adiabatic results are also applicable for use in fuel cells and micro chemical reactors and biological MEMS devices where gas venting is of great interest. The diabatic vapor venting results help provide a clearer picture of the impact of phase change in a vapor venting channel and is included to highlight some of the key features of vapor venting flow regimes that are not manifested during adiabatic operation. The different flow regimes and transient flow regime behavior in comparison to those encountered during adiabatic flow can impact both the pressure drop and heat transfer in the microchannel. The diabatic experiments also capture the fact that unlike air injection studies, vapor is generated throughout the device, and this can impact the spatial evolution of the flow regime as well as the total vapor removal rates. The observed diabatic flow regimes also help explain some of the thermal and hydraulic characteristics observed in a bulk vapor venting copper microchannel heat exchanger, discussed in detail by David et al. (accepted for publication).

The following section, Section 2, discusses the device fabrication and experimental setup, Section 3 presents the adiabatic and diabatic visualization results and analysis and is followed by Section 4, which provides some design recommendations based on the findings.

## 2. Experimental method

### 2.1. Device design and fabrication

The device is designed to provide visualization of adiabatic air and diabatic vapor venting from two-phase flow produced by the injection of air into a water stream and by heating respectively. All the materials used in the fabrication were chosen to be thermally stable up to 125 °C. The cross-sectional and top views of the copper microchannel device are shown in Fig. 1. The device is assembled from four separate pieces, labeled 1 through 4, that are screwed together with the membranes sandwiched between the liquid and vent halves of the device. The copper bodies, pieces 1 and 3, are made from electronics grade, polished copper with the microchannels end-milled with a high precision CNC facility. The liquid microchannel, machined in piece 1, has a length of 24 mm, a width of 124 μm and a depth of 98 μm (hydraulic diameter = 110 μm). The air injection channel, also machined in piece 1, is 2.5 mm long, 132 μm wide and 40 μm deep, with a hydraulic diameter of 62 μm. The air injection port needs to have a small hydraulic diameter to approximate a bubble nucleation site. The air injection channel intersects the liquid channel 6 mm from the liquid inlet. The vent microchannel, machined in piece 3, has a length of 24 mm, a width of 140 μm and a depth of 150 μm, with a corresponding hydraulic diameter of 145 μm.

The gas/vapor separation membrane that faces the liquid carrying microchannel is an isotropically porous, unlaminated, hydrophobic Teflon membrane with a 220 nm effective pore diameter and a thickness of 65 μm ± 5 μm (Sterlitech Corp., WA, USA and GE Osmonics, MN, USA). This hydrophobic membrane allows transfer of the gas phase but holds back the liquid phase through surface tension forces. Assuming straight capillary pores and using the Young–Laplace equation the leakage pressure for the liquid phase is given by Eq. (1) (Meng et al., 2007),

$$\Delta P = \frac{4 \cdot \sigma \cdot \cos(\pi - \theta_{adv,max})}{d} \quad (1)$$

where the surface tension, $\sigma$ = 0.072 N/m, the advancing contact angle for water on Teflon, $\theta_{adv,max}$ = 123° (García-Payo et al., 2000) and manufacturer stated pore diameter, $d$ = 220 nm. The liquid breakthrough pressure for the Teflon membrane is found to be in excess of 700 kPa. The maximum pressure encountered in our current experiments is less than an eighth of this value. A mechanically stiff, hydrophilic, carbon-mesh membrane (Toray Carbon Paper, courtesy of Honda Corp, Japan) with isotropic pores of diameters in the order of 10's of microns and a thickness of 170 μm ± 10 μm is added to

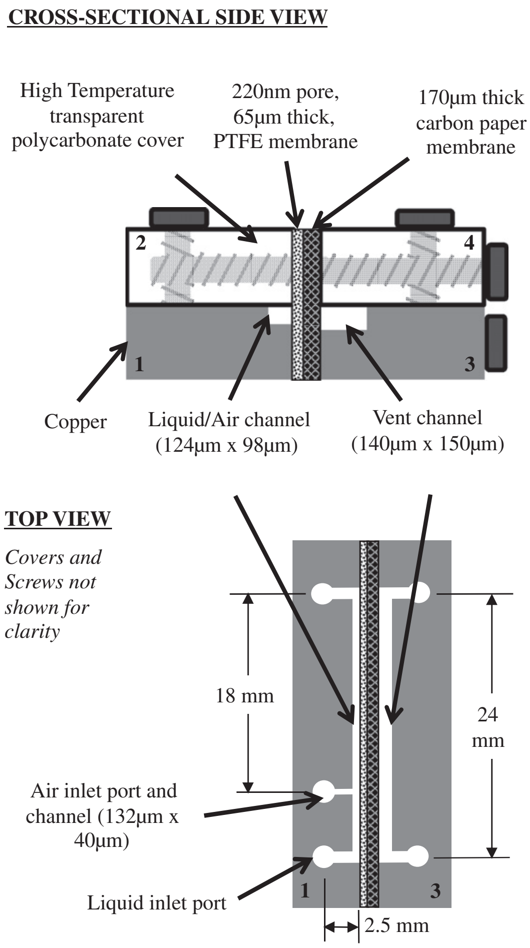


**Fig. 1.** Cross-sectional side and top views of the copper microchannel device (figures are not to scale).

provide mechanical support and stop the membrane from deforming and impeding visualization of the venting process.

### 2.2. Experimental setup

The experimental setup for the adiabatic experiments is shown in Fig. 2. Distilled water, filtered through 0.5 µm and 20 nm in-line filters, is pumped into the device using a Shimadzu LC-10AD peristalsis pump. Liquid inlet pressure is measured using an Omega PX219-30V45G5V pressure sensor with an accuracy of 1 kPa. Liquid inlet flow rate is measured using a Sensirion SLG1430-24 flow meter with an accuracy of 10% of the measured value. Air, filtered through a single 20 nm in-line filter, is pumped into the device through the air injection port using a syringe pump fitted with a 100 ml glass syringe. Air pressure is measured using an Omega PX01C1-015G5T pressure sensor with an accuracy of 0.2 kPa. Air volumetric flow rate is measured using a Sensirion CMOSense EcoLine EM1NL gas flow meter with an accuracy of 0.15 ml/min. All thermocouples used are Omega 40 gauge, type K thermocouples and were converted to millivolt signals using Fluke 80TK and Omega SMCJ-K thermocouple-to-voltage converters. The pair of IR slot sensors is used to determine interface velocities of air slugs in the outlet tubing. The slot sensors are composed of an IR emitter and detector. The transparent plastic tubing is inserted between the emitter and detector. Due to the difference in the angle of refraction between the plastic and the gas or water, the amount of IR radiation detected varies with the presence of gas or liquid in the tubing. The distance between the sensors is 6.45 mm and for a sampling rate of 200 Hz can resolve interface velocities up to 1.29 m/s. By measuring the front and back interface velocities of the air plug as well as the total residence time, the volume of each air slug and the air flow rate in the outlet tubing can be determined. The clamp on the outlet tubing allows us to raise the total static pressure of the device. For the diabatic experiments, the air injection port is blocked and the air-injection equipment is not used. Vapor is generated by uniformly heating the side opposite the visualization surface with a 10 W Kapton heater. Device temperatures were measured approximately half way along the main channel using a thermocouple. The parasitic heat loss for each flow rate was estimated from inlet and outlet fluid temperatures obtained during sensible heating of the fluid. This heat loss was found to be approximately 73% at the mass flux of 140 kg/s/m$^2$ and 52% at the mass flux of 340 kg/s/m$^2$. The large heat loss was due to the comparatively small surface area in the channel involved in forced convective heat transport as compared to the exposed surfaces of the device through which conductive (fixturing) and free convection losses occur. This calculated heat loss was applied during two-phase flow to estimate the thermodynamic exit quality, $x_e$, as given by Eq. (2), where $m$ is the mass flow rate of liquid, $C_p$ the heat capacity and $\Delta H_{fg}$ the latent heat of vaporization.

$$x_e = \frac{(1 - q_{loss\ frac}) \cdot q_{in} - \dot{m} \cdot C_p \cdot (T_{sat} - T_{in})}{\dot{m} \cdot \Delta H_{fg}} \tag{2}$$

Empirical simulations of two-phase flow in copper devices as well as previous experimental work by authors such as Steinke and Kandlikar (2004) suggest that for devices such as the one presented in this work the channel wall boundary lies between a constant heat flux and constant temperature boundary condition.

For adiabatic air-injection flows the initial inlet quality, $x_i$, is calculated using Eq. (3) where $m_{liq}$ is the liquid mass flow rate and $m_{air}$ is the air mass flow rate calculated from the volumetric flow rate and pressure dependant density.

$$x_i = \frac{\dot{m}_{air}}{\dot{m}_{air} + \dot{m}_{liq}} \tag{3}$$

Videos of the flow structures in the microchannel were recorded using a Vision Research Phantom v7.3 high-speed camera at rates of 5000–20,000 frames per second. Voltage data from the thermocouples and pressure sensors is collected through a NI SCB-100 breakout box connected to an E-series NI DAQ card. Numeric data from the Sensirion flow meters were collected through two COM ports. Data and image collection were carried out on two separate computers but were triggered simultaneously using LabView. Baseline data was collected at the beginning of every experiment to correct for any offsets in the sensors. Single-phase liquid flow data was collected at several flow-rates to determine the single-phase hydraulic resistance per unit length of the liquid channel.

### 2.3. Single phase Poiseuille number and Nusselt number

The Poiseuille number is defined as $Po = 0.25 * f * Re$, where $f$ is the Darcy friction factor. The theoretical $Po$ number for our channel is calculated to be 11.2 using the series solution for a rectangular duct as described in White (1991). From measurements of the single phase pressure drop at water flow-rates of 0.05, 0.1, 0.25 and 0.5 ml/min, the average experimental hydraulic resistance (pressure drop/vol. flow rate) is found to be 7.8e4 Pa/ml/min, and the average Poiseuille number to be 11.0. Thus the experimental measurements show good agreement with the theoretical calculations.

The theoretical Nusselt number for a rectangular channel with width/depth ratio of 1.26 is determined to be 3.68 for constant heat flux boundary condition and 3.04 for constant temperature

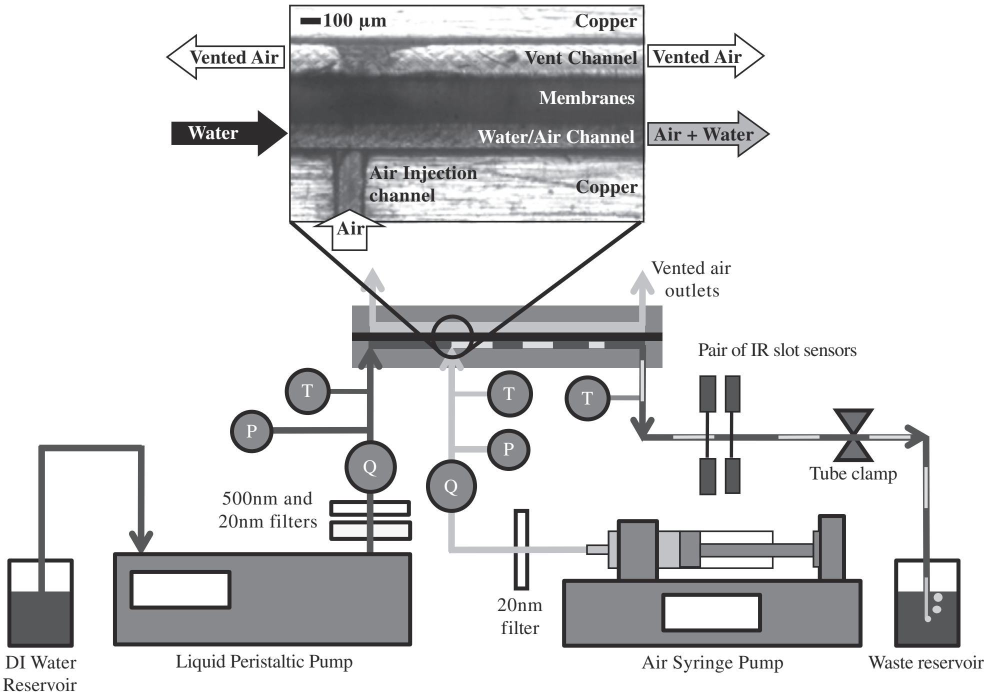


**Fig. 2.** Experimental setup showing key equipment and close up of channel. *T* represents a thermocouple, *P*, a pressure sensor and *Q*, a flow meter. Liquid is pumped using the peristaltic pump and air is delivered by the syringe pump. The vent side of the channel is left open to the atmosphere. Non-vented air flow rate in the outlet tubing is measured using the pair of IR slot sensors that measure air slug velocities and residence times.

boundary condition (Kays and Crawford, 1993). With the assumption of a constant wall temperature boundary condition, the experimental Nu number is found to be only 0.4 and 1.8 at 0.1 and 0.25 ml/min flow rates respectively. Some contributing factors for this large discrepancy might be: (i) only 2 of the 4 walls are heated in the experiment which would result in the Nu number being smaller than theoretically predicted, (ii) actual effective heat transfer area may be smaller than currently calculated if spreading in the substrate resulted in much of the heat being absorbed by the fluid in the initial developing region of the channel.

## 3. Results and discussion

### 3.1. Adiabatic air–water flow

#### 3.1.1. Visualization of flow-regime

An example of adiabatic air venting through the membrane is shown in Fig. 3, where the air velocity is 0.32 m/s ($5.6 \times 10^{-9}$ kg/s) and the liquid velocity is 0.36 m/s ($4.3 \times 10^{-6}$ kg/s). The sequence shows a bubbly type flow that is typically observed at low inlet air flow rates with the size of the bubbles increasing with air injection velocity. Bubbly type structures were also often observed downstream at the tail end of many of the other flow structures, which we attribute to the reduction of superficial air velocity due to air venting through the membrane.

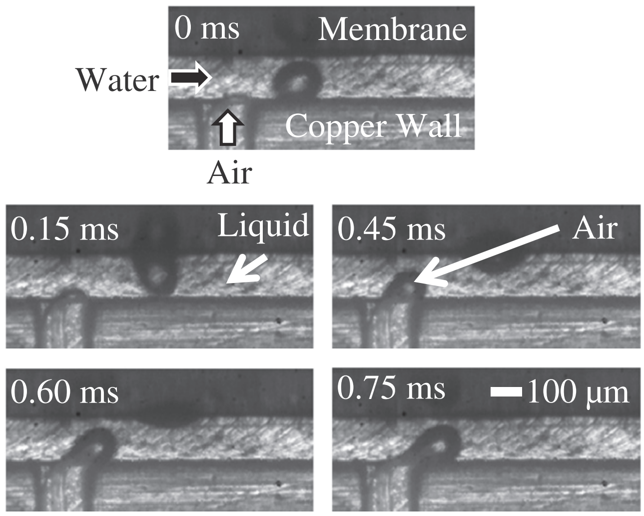


**Fig. 3.** Sequence of images showing an example of bubbly air venting at a liquid velocity of 0.36 m/s and an air injection velocity of 0.32 m/s. As air is injected into the liquid stream, small bubbles break off the injection port (0 m s) and attach to the membrane (0.15 m s) through which the air can now escape causing the bubble to collapse (0.15–0.6 m s) until it eventually disappears (0.75 m s). As air flow rate is increased the bubbles get larger and move along the membrane surface once attached.

Fig. 4 provides examples of the other major types of flow structures that were observed near the air injection port during the experiments and Fig. 5 summarizes these observations on a superficial velocity regime map. For the liquid velocity range of 0.1–0.15 m/s, as air velocity is increased to approximately 1.2 m/s, the structure changes from bubbly to wavy (Fig. 4A) where the wavy flows are essentially several large static coalesced bubbles. As air velocity is increased to approximately 5.2 m/s we see a mixed wavy-stratified/stratified type flow that transition from regions that start wavy-stratified, smooth out downstream and then end with a region of waviness and bubbly type flow. The waviness near the injection is due to the initial interaction between the air stream, the liquid stream and membrane, with the air velocity not sufficiently high to allow the air to uniformly spread across the membrane. At air velocities of 5.2 m/s and above, smooth stratified flows are observed which then transition to wavy-stratified flows downstream (Fig. 4B). Stratified flows are only typically observed in horizontal macrochannels due to gravity but are produced here due to surface tension. Due to the asymmetric

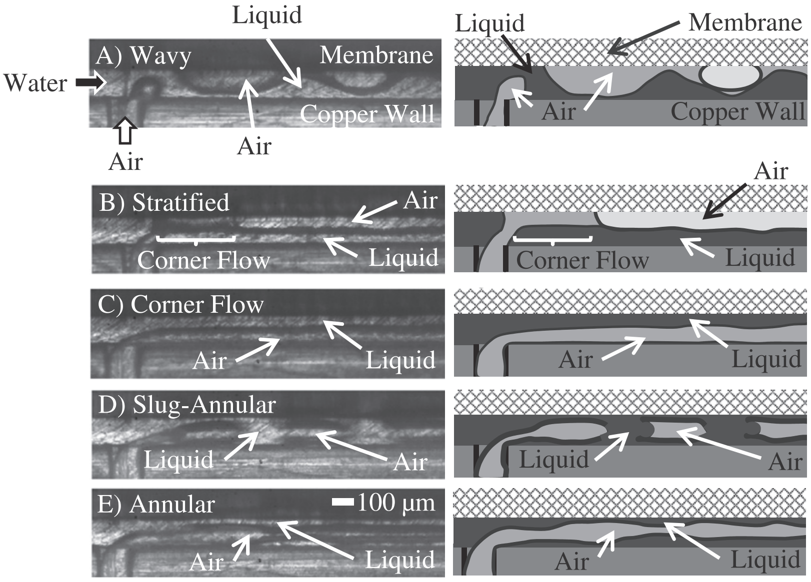


**Fig. 4.** Examples of steady state flow structures that were observed at different air and water velocities. (A) Wavy flow, (B) stratified flow, (C) corner-wedge flow, where the flow structure forms on the plastic–copper corner, (D) slug-annular flow and (E) annular flow. The latter two flow regimes are observed at the highest tested Weber number of 0.6.

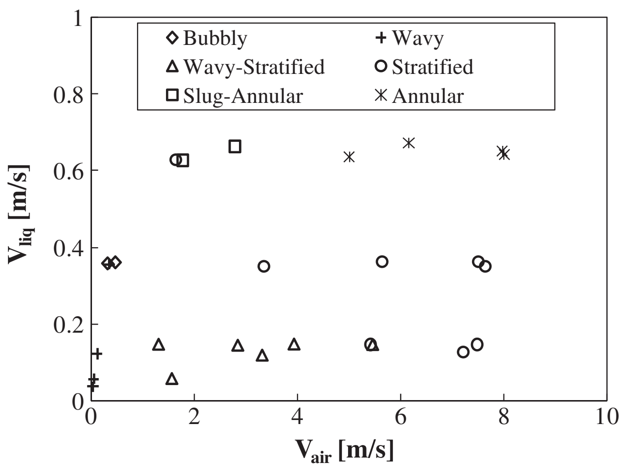


**Fig. 5.** Superficial velocity flow regime map for adiabatic air–water two-phase flow in a microchannel with one porous hydrophobic wall.

structure of the injection port, a corner wedge type flow can be seen in the initial part of the stratified flow. The corner wedge flow appears darker due to the curvature of the interface in the depth-wise direction. Once the air contacts the bottom copper surface the interface straightens out resulting in a brighter region and a clearer, more distinct, interface between the liquid and the air.

In the case of liquid velocities in the range 0.35–0.36 m/s, the structure transitions from bubbly to stratified flow as air velocity is increased. The corner wedge structure (Fig. 4C) also occasionally manifests itself at the highest tested air velocity of 7.55 m/s, flowing along the plastic–copper corner rather than the plastic–PTFE corner as seen in Fig. 4B. This corner wedge structure spatially transitions to a regular stratified flow downstream, with the air now flowing along the membrane. The location of the transition varied, but occurred within 3 mm of the air-injection port.

At the highest liquid velocity of 0.63–0.67 m/s, we again occasionally observed the corner wedge structure which at the lowest air velocity of 1.6 m/s spatially transitions directly to a regular stratified flow, but on slight increase to 1.8 m/s, transitions to slug and then bubbly flows on the membrane instead. As air velocity is increased from 1.8 to 2.8 m/s, annular-slug (Fig. 4D) structures first become dominant and then, at velocities greater than 5 m/s, changes to more continuous annular structures (Fig. 4E). The spatial transition of these annular flows to stratified and bubbly flows occur several millimeters downstream and increases with the superficial air velocity. For many of the observed flow regimes described, particularly for those obtained at superficial air velocities <4 m/s, all the injected air was vented through the membrane, leaving single phase liquid at the outlet of the microchannel.

In general, traditional two-phase flow regimes maps developed for mini and macro scale channels (with diameters larger than a millimeter or so), such as the widely adopted map and transition criteria developed by Taitel and Dukler (1976) for gas–liquid flow in horizontal channels, cannot be applied for two-phase flow in microchannels due to the impact of surface tension and confinement effects (as indicated by small Bond numbers), which lead to differing flow regimes. This is described in greater detail along with a comprehensive summary of previous work in the development and application of two-phase flow regime maps by Cheng et al. (2008). Chung and Kawaji (2004) and Cubaud and Ho (2004) are recent examples of adiabatic microchannel flow visualization and regime map development. Chung and Kawaji considered flow in circular glass capillaries of diameters ranging from 50 μm to 526 μm, with two phase flow generated by injection of nitrogen into the water stream at a mixer. They found that flow regimes observed in the 250 μm and 526 μm diameter capillaries were different from those observed in smaller 100 μm and 50 μm capillaries. Cubaud and Ho looked at two-phase air–water flow in rectangular, serpentine silicon channels of hydraulic diameters 200 μm and 525 μm and found a unique wedging type flow with liquid flowing along the corners of the channels.

To more closely mimic gas/vapor formation in real devices such as fuel cells and heat exchangers the air injection in our device is asymmetric, using a T-junction, which can lead to differing flow regimes as compared to coaxial liquid injection, as was used by Cubaud and Ho (2004) and Chung and Kawaji (2004) making a direct comparison between their observations and ours less appropriate.

As experimentally observed by Garstecki et al. (2006) and simulated by De Menech et al. (2008), T-junction injection can lead to differing flow regimes with 'squeezing' type flows at low Capillary numbers (seen in Fig. 3), 'dripping' flows at intermediate capillary numbers and 'jetting' type flows (seen in Fig. 4D and E) at higher capillary numbers. Though a comprehensive flow regime map for T-junction two-phase flows is not currently available, the work of Garstecki et al. and De Menech et al. indicate that the liquid capillary number and the velocity ratios of the continuous and dispersed gas phase play an important role in the type of flow generated. The size of the structure is dependent on the velocity ratio, with $V_{air}/V_{liq} < 1$ leading to smaller bubbles and $V_{air}/V_{liq} > 1$ generally leading to larger structures as seen in Fig. 5. The capillary number on the other hand determines the type of breakup that occurs as described above. Pressure mediated breakup at low capillary numbers is not considered to be as significant in our work since the depth of the injection port is smaller than that of the main channel and the air structures do not fill the cross-section of the channel as they grow. The 'squeezing' type breakup is only observed during bubbly flow at $V_{air}/V_{liq} \sim 1$ and Ca = 0.005, about a factor of two smaller than suggested by Garstecki et al. (2006). Higher velocity ratios and the hydrophobicity of the membrane help stave off breakup at higher velocity ratios by creating 'bridges' of gas connecting the injection port to the membrane. 'Jetting' flow leading to annular-slug and annular flows structures occurs begins in the range 0.005 < Ca < 0.009 where the liquid velocity is now sufficiently high to stop the injected air column from reaching the membrane and causing it to breakup downstream. This type of breakup is less amenable to gas venting as it leads to the gas being surrounded by liquid films that stop the gas from reaching the membrane and venting.

### 3.1.2. Air-venting analysis

A closer analysis of venting area, Weber number, flow-regime and static pressure on air venting rates reveal useful design guidelines for heat exchangers and other gas venting devices. The choice of the appropriate dimensionless parameter for liquid flow can be determined from the relative magnitude of the Weber, Capillary and Reynolds numbers. For liquid velocities of 0.14, 0.36 and 0.65 m/s, the Weber number (≈inertia/surface tension) is determined to be 0.03, 0.2 and 0.6, the Capillary number (≈viscous/surface tension) is 0.002, 0.005 and 0.009 and the Reynolds number (≈inertia/viscous) is 15, 38 and 70. Since surface tension forces > inertial forces > viscous forces, we choose the Weber number, $We = \rho V_{liq}^2 D_h/\sigma$, where $\rho$ is the density of the liquid, $\sigma$ is the surface tension and $D_h$ is the hydraulic diameter of the main channel, as the dimensionless parameter of interest for liquid flow.

Fig. 6 highlights the role of Weber number and flow structure on the air venting rate at different pressures. At low inlet air flow rates where the two-phase pressure drop at the injection point is less than 20 kPa, bubbly and wavy type flows dominate and result in complete venting of the injected air. As air injection at the two lower liquid velocities increase, the mass quality increases and results in an increase in the two-phase pressure drop. The flow-regime also changes to wavy-stratified and stratified. At the highest flow velocity and Weber number, annular type flows are dominant. Annular type flows require a much larger pressure to vent a given amount of vapor as compared to the lower Weber number flows and the increase in air removal rate with pressure (slope of the curve) is smaller than for the two lower liquid velocities.

Figs 7 and 8 help explain the behavior observed in Fig. 6 and also delineate the role of venting area to the venting performance. Points marked *, #1 and #2 in these figures and in Fig. 9 are special flow circumstances that is discussed at the end of this section. Fig. 7 considers the impact of the Weber number and quality on

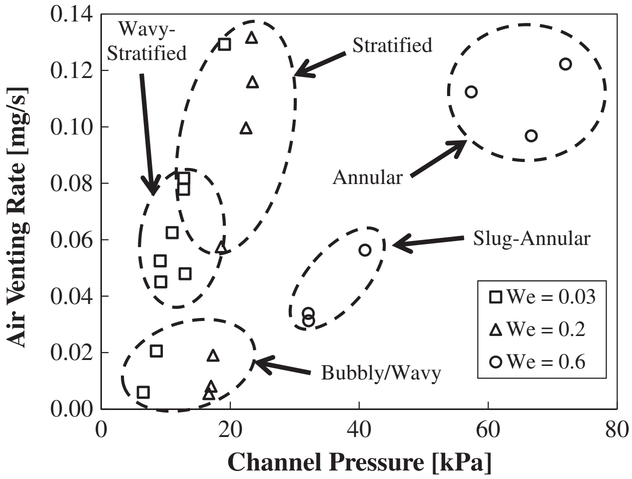


**Fig. 6.** Air venting rate vs. pressure as measured at the air injection port. The type of flow-regime experienced influences the rate of air removal through the membrane. At the two lower Weber number flows, most of the air injected is removed but this is not the case at the higher Weber number flow, where differing flow regimes and partial venting result in higher pressure drops.

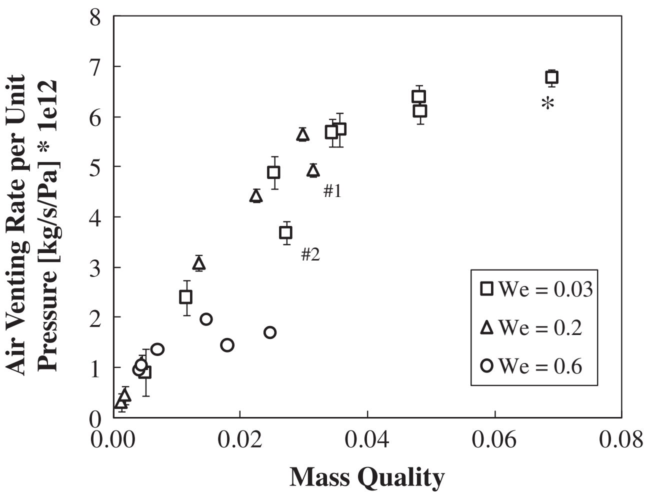


**Fig. 7.** Air venting rate per unit injection point pressure (venting effectiveness) vs. mass quality. The poor effectiveness of the highest Weber number flow is clearly seen with a roll-off of around $2 \times 10^{-12}$ kg/s/Pa as compared to $6 \times 10^{-12}$ kg/s/Pa for the lower Weber number flows. High Weber number flows can result in less desirable corner-wedge (#1) and annular type flows that delay venting and reduce the maximum venting effectiveness.

the venting rates by looking at the venting rate per unit system pressure (as measured at the T-junction) as the inlet quality is increased (by increasing the air injection rate). The venting rate per unit pressure, i.e. the venting effectiveness, should be maximized. As mass quality increases, there is initially a linear increase in the venting effectiveness followed by a roll-off as the venting effectiveness is maximized. For the low and intermediate flow rates this roll-off occurs at around $6 \times 10^{-12}$ kg/s/Pa. However, for the higher Weber number flow the roll-off occurs much lower at around $2 \times 10^{-12}$ kg/s/Pa. A plot of the normalized venting area with the quality, shown in Fig. 8, indicates that the slope and roll-off in Fig. 7 is related to the venting area. The venting area is the contact area between the air structure and the membrane and is estimated from the images. This venting area increases linearly with quality until a value of 3% at which point all the available area has been utilized and air begins to appear in the outlet tubing. The roll-off

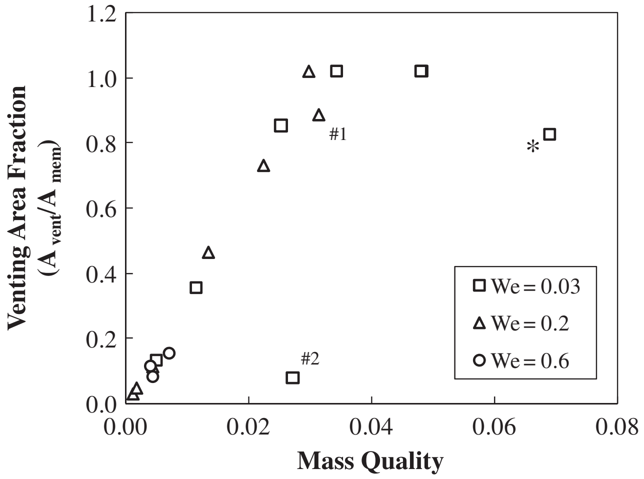


**Fig. 8.** Normalized venting area vs. mass quality. Contact area between air and membrane increases linearly with quality until all area has been utilized. At this point, the venting effectiveness is maximized and further venting occurs only if pressure is increased. At increased trans-membrane pressures (*), upstream venting rate increases, freeing more space for further venting.

in Fig. 7 occurs at approximately the same quality and the slope of the linear region in Fig. 7 is found to be equal to $B \times A_{vent}$ where $B$ is a constant. Thus venting effectiveness continues to rise as long as there is area to vent through and is maximized when all the area has been used up. At the highest Weber number, where inertial forces are now becoming increasingly more important, the formation of long annular air structures at qualities >1% impedes the air structures from contacting the membrane until much further downstream resulting in a much smaller total venting area seen by the air before reaching the outlet manifold. This results in the lower roll-off as seen in Fig. 7. These plots indicate that as long as the air-structure does not result in separation of the gas phase from the membrane then the venting effectiveness is insensitive to the Weber number under the tested conditions. The Weber number is important, however, as it determines the manner of breakup of the dispersed gas phase during injection, which in turn determines how effectively the gas phase is brought into contact with the membrane. From a gas/vapor venting device design standpoint, it is important to maximize the total potential interaction area between the gas/vapor phase and the membrane, thus increasing the amount of gas/vapor a channel can support before its venting effectiveness is maximized. For a gas venting device it is also important to design the system for smaller Weber numbers to avoid the formation of annular type flow structures. This design rule does not necessarily apply for thermal vapor venting devices, as discussed in Section 3.2.

Since the slope of the linear region in Fig. 7 is directly related to the venting area, assuming Darcy flow in the membrane, the venting rate per unit area per unit pressure must be a constant and equal to the membrane and fluid properties. To verify this it is necessary to determine the actual pressure experienced by the air structure. To determine this driving pressure, we measured the position and length of the venting structure, and then eliminated the single-phase liquid pressure contribution in the section upstream and downstream of the structure using the experimentally determined single-phase hydraulic resistance. We use the mean of the pressure across the structure as the driving pressure for venting, assuming that the pressure varies linearly along the structure. In the case of smaller bubbly type flows where curvature is significant, we incorporated the additional Laplace pressure with an average radius estimated from images taken during venting. Since the PTFE separation membrane is isotropic and the exposed areas on either side of the membranes are not equivalent (see Fig. 1) we include a spreading effect in the determination of the venting area, with the dimension of the venting footprint (approximated as a rectangle) increased by half the thickness of the membrane stack. The venting footprint 'rectangle' assumes that the air structure stretches depth-wise through the channel which is valid in most wavy and stratified flows and some larger bubbly flows. The result of the calculations is shown in Fig. 9. The venting flow rate per unit area per unit pressure is almost a constant for the tested mass qualities but shows a slight upward trend with quality, believed to be due to an increasing underestimation in the venting area when the structure spans a large fraction of the channel. To compare this result with the membrane permeance, we used the experimentally determined value for the intrinsic permeability of the Teflon 220 nm membrane of $5 \times 10^{-15}$ m$^2$ (5 milli-Darcy), documented by Marconnet et al. (2008), and determined the theoretical membrane permeance to be $4.1 \times 10^{-6}$ m/s/Pa ± $1.1 \times 10^{-6}$ m/s/Pa using

$$\Phi_{mem} = \frac{Q_{air}}{\Delta P \cdot A} = \frac{K_{mem}}{t_{mem}} \cdot \frac{1}{\mu_{air}} \tag{4}$$

The membrane permeance, $\Phi_{mem}$, assuming single-phase Darcy flow in the membrane, depends on just the thickness of the membrane, $t$, its intrinsic permeability, $K$, and the fluid dynamic viscosity $\mu$. The intrinsic permeability depends on the structure of the pores, the porosity and typically scales with the square of the pore diameter. Since the intrinsic permeability of the carbon mesh support membrane varies between $1 \times 10^{-12}$ m$^2$ and $12 \times 10^{-12}$ m$^2$ (Pasaogullari et al., 2007; Sinha et al., 2007), its contribution to the total permeance is neglected. The agreement between the current results and that theoretically predicted using Eq. (4) emphasizes that air venting is fundamentally limited by the membrane properties and it is important to choose a membrane that is both thin and has high gas/vapor permeability.

To study the impact of trans-membrane pressure on the venting performance we tightened the clamp shown in the setup in Fig. 2 to increase the static pressure on the two-phase side of the device. The trans-membrane could also be increased by adding a vacuum to the vent channel on the other side of the membrane. The increase in static liquid pressure resulted in the data point indicated by the star ($*$) in Figs. 7–9. The rise in pressure increases the air

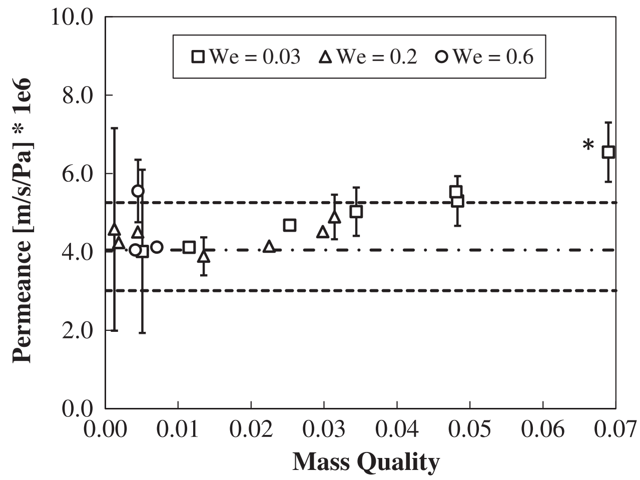


**Fig. 9.** The venting rate per unit area per unit pressure (permeance) generally matches the theoretically calculated value of $4.1 \times 10^{-6} \pm 1.1 \times 10^{-6}$ m/s/Pa (–·– and - - respectively). The theoretical value is determined from the membrane thickness and intrinsic permeability measurements (Marconnet et al., 2008).

vented at every point in the venting structure, causing the air structure to shorten and recede back upstream, reducing the normalized venting area from 1 to 0.8 as seen in Fig. 8. In Fig. 7, this would result in a higher roll-off, since the higher static pressure in the device has freed up more venting area. Thus, we could increase the maximum venting effectiveness by increasing the trans-membrane pressure.

The point marked #1 in Figs. 7–9, had a long 2.5 mm corner-wedge flow before transitioning to a stratified flow. The corner flow is not ideal for venting by reducing the potential venting area as seen in Fig. 8, and the venting effectiveness rolls-off at a slightly lower value than expected for the given Weber number and quality in Fig. 7. The other data-point of interest, marked #2 in the previous figures, indicates an unusual flow regime, where instead of developing a stratified flow, the structure instead resembled a short corner-wedge flow followed by bubbly/slug type flow. This flow structure was only observed once during testing.

### 3.2. Diabatic vapor–liquid flow

#### 3.2.1. Visualization of flow-regime

Though the adiabatic visualization and analysis provides useful insight for gas and vapor venting devices it is valuable to consider the types of flow regimes encountered during phase change and how they might specifically inform heat exchanger design. Figs. 10 and 11 provide examples of the flow regimes that were observed during diabatic operation. With an average mass-flux velocity of 140 kg/s/m$^2$ and thermodynamic exit quality of less than 1%, the flow structures are initially bubbly type flow (Fig. 10A) with individual bubbles nucleating and growing on the copper surface and then venting through the membrane, similar to the adiabatic venting sequence shown in Fig. 3. As the wall heat flux and thus quality increases, we see slug type flow (Fig. 10B) with a distinctive asymmetric front and back interface due to the non-wetting hydrophobic membrane. When the quality exceeds 1%, stratified flow becomes dominant (Fig. 10C) with the liquid film thickness reducing as the heat flux and quality increases. We also observed bubble nucleation and growth within the stratified region with the bubble breaking through the liquid film and merging with the vapor film once it has grown large enough. As quality increases further we begin to observe a cyclical stratified flow. This cycle initially starts with a wetting phase where liquid slugs initially wet the copper surface, followed by the establishment of the stratified flow structure. Over time the film thickness in this stratified region gradually reduces until eventually there is a dry-out period where there is only vapor flowing through the channel at the observed location. At the highest tested quality of 10% this cycle was found to last approximately 0.1–0.12 s. This cyclical behavior has been experimentally observed in microchannels and the process described by Kandlikar (2004) and modeled by Thome et al. (2004). However, in these and other previous work in this field, the cyclical process involves a liquid only period, followed by a period of annular flow with thinning liquid films followed by a dry region. Due to the hydrophobicity of the membrane in our channel, the annular region is replaced with a stratified region, and liquid slugs that fill the entire cross-section are replaced with liquid droplets travelling on just the wetting surfaces.

For the liquid mass flux of 340 kg/s/m$^2$, at low heat fluxes and qualities, we observe larger bubbly type vapor structures that, unlike the smaller bubbles formed at the lower mass flux, form on the membrane rather than the copper surface (Fig. 10D). This may be due to growth of vapor pockets in the membrane due to evaporation. If the rate of vapor removal through the membrane is smaller than the rate of vapor generation in these vapor pockets then they would grow into the channel as observed. Stratified flow is observed at higher heat fluxes and qualities similar to the lower flow-rate but the liquid films are generally thinner with liquid also flowing as droplets on the membrane surface. In the quality range between 6% and 11% we begin to see cyclical behavior, but the flow structures are quite different from the lower-flow rate case. The cycle begins with wetting liquid rivulets and drops flowing not just on the copper surface but on the plastic and membrane surfaces

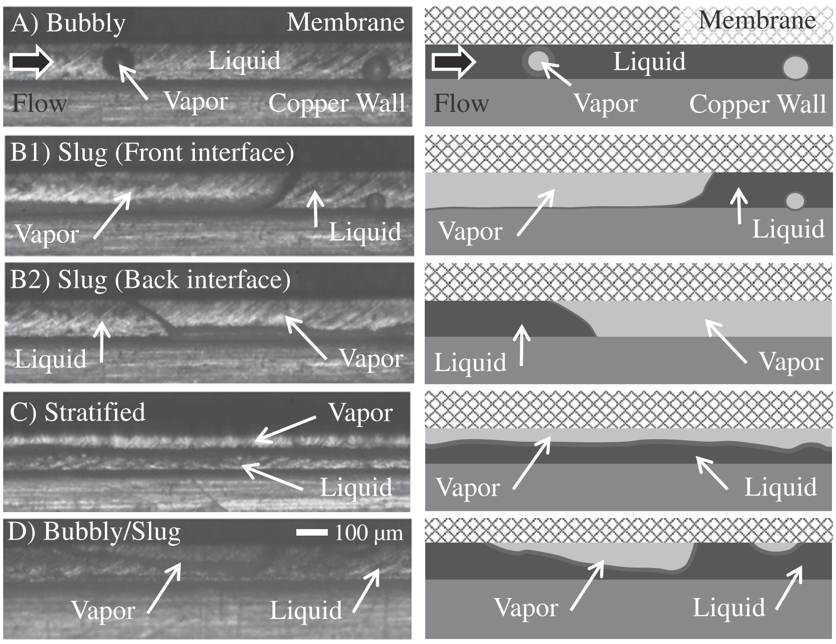


**Fig. 10.** Examples of the dominant flow regimes observed during diabatic operation with the black arrow indicating direction of liquid flow. (A) Bubbly flow is typically observed at very low mass qualities <1%. (B) Slug type flows are also only observed at low qualities and have a distinctive asymmetric shape due to the hydrophobicity of the membrane. (C) Stratified flows are dominant at intermediate qualities up to 10% with cyclical wetting-stratified-dryout behavior observed at $G$ = 140 kg/s/m$^2$ and qualities >4%. (D) At the higher mass flux of 340 kg/s/m$^2$ and at low qualities larger bubbles are observed forming on the membrane, then coalescing to form stratified and slug flows.

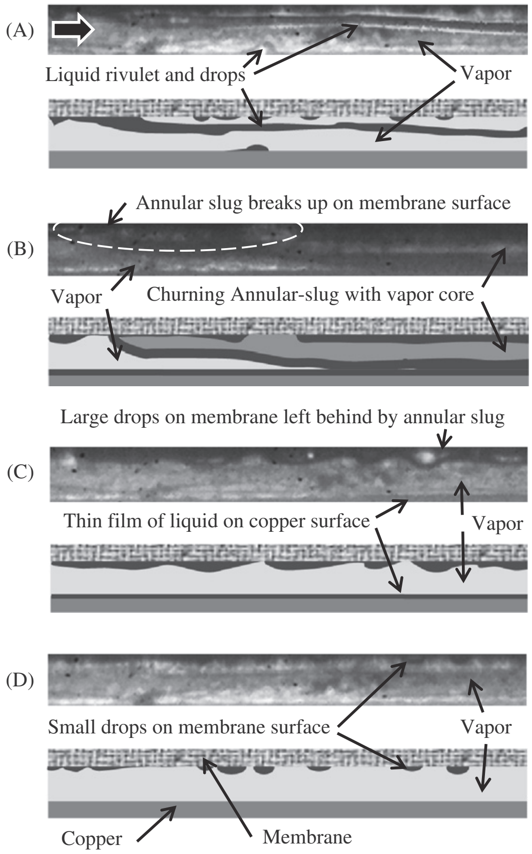


**Fig. 11.** Sequence of images at various times during cyclical churn-annular flow that is observed only at the higher mass flux of 340 kg/s/m$^2$ and at qualities >10%. Schematics are drawn directly from the images and are included for clarity. Movie is available on request. Initial wetting by liquid rivulets occurs on the various surfaces (A) followed by several churning annular slugs (B). These churning annular structures appear to breakup on the membrane surface leaving behind large droplets (C) most of which coalesce and are pushed out leaving behind smaller drops during the dry-out phase when the thin liquid films on the wetting surfaces evaporate (D). The entire cycle then repeats and found to vary from 0.02s to 0.1s ($f \sim$ 10–50 Hz).

as well (Fig. 11A). This initial period is then followed by a short period of churning annular type flow (Fig. 11B) with a vapor core surrounded by a liquid film. The thin liquid film in contact with the membrane breaks up, with the liquid beading up to leave distinct liquid droplets on the surface of the membrane (Fig. 11C), and liquid films on the wetting surfaces that evaporate over time. Several more periods of this churning annular slugs (as many as a dozen) follow, both removing and leaving new droplets on the membrane and replenishing the liquid films, until eventually a long dry-out period is achieved (Fig. 11D) during which the thin films almost completely evaporate. The entire cycle then repeats as liquid upstream overcomes the increased pressure in the channel due to vaporization and rewets the channel. The liquid droplets, depending on the size, number and contact with the copper and plastic wetting surfaces, either remain on the membrane until the next cycle or coalesce to form larger drops that are then pushed out. At the highest tested quality of 20% the cycles were found to last between 0.02 and 0.1 s in duration.

A diabatic flow regime map for the data is shown in Fig. 12. The low quality flow regimes of bubbly, slug and plug type flows are not included because they cannot be accurately associated with a particular quality due to lack of spatial data. Comparing with the adiabatic visualization and data points plotted in Fig. 12, we see that in the diabatic case the wavy, wavy-stratified, corner-wedge or smooth annular flows are not observed. Hetsroni et al. (2005)

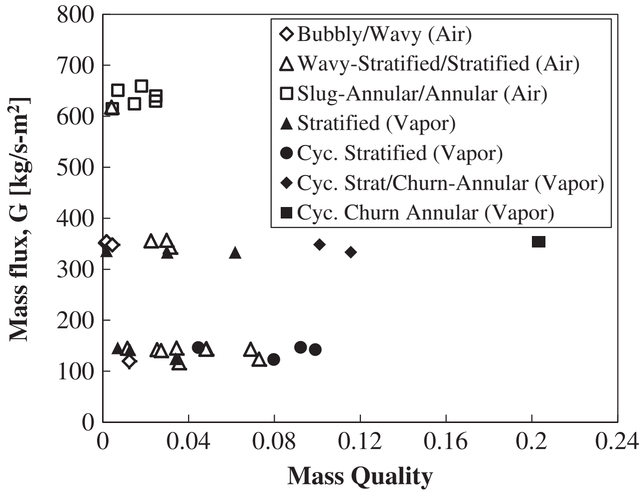


**Fig. 12.** Diabatic flow regime map for the vapor separation microchannel at the two tested mass fluxes. At $G$ = 140 kg/s/m$^2$ stratified and then cyclical stratified flows are observed and at $G$ = 340 kg/s/m$^2$, stratified type flows give way to a cyclical mixed stratified and churning-annular type flow which then leads to cyclical churn-annular type flows at higher qualities. In general the flows at the higher mass flux were more chaotic.

and more recently Harirchian and Garimella (2009) provide visualization of the different types of diabatic flow regimes encountered in two-phase water and refrigerant flow in microchannels. Harirchian and Garimella (2010) and Revellin and Thome (2007) also develop new transition criteria, using refrigerant data, to describe the changes in flow regime with the Bond number, Boiling number, Reynolds number and Weber number, which together capture the effect of inertia, heat flux and confinement effects in the microchannels. The impact of increasing heat flux on the flow regime is shown in Fig. 12 and discussed in the given references and can be considered under two cases: (i) at constant mass flux and (ii) at constant flow quality. Increasing heat flux at a fixed mass flux leads to flow transitioning from bubbly/slug type flows to annular and stratified (with the hydrophobic membrane) type flows. As heat fluxes continue to rise, partial dryout, and finally complete dryout is observed. In the second case, to maintain a fixed flow quality with rising heat flux, the mass quality must rise. As heat flux and mass flux increase the flow transitions from well behaved, simple flows such as bubbly and smooth annular to increasingly more chaotic flows such as churn annular and churn stratified flows, as seen when comparing the flow regimes at 140 kg/s/m$^2$ and 340 kg/s/m$^2$.

Fig. 13 shows our data plotted on the flow regime map proposed by Harirchian and Garimella (2010) along with their transition criteria,

$$Boi \times \mathrm{Re} = 0.017(Bo^{0.5} \times \mathrm{Re})^{0.7} \quad (5)$$

where $Boi$ is the Boiling number and $Bo$ is the Bond number. Below the line, they found the flow was primarily confined slug flow and above the line, churn and confined annular type flows. Their prediction of churning annular flow is consistent with our data. Below the transition line we find stratified flow to be dominant along with both bubbly and slug flows at very low qualities. The existence of stratified flow and bubbly flow is not surprising as the hydrophobic membrane encourages the confined vapor slugs to spread out and 'wet' the membrane, forming bubbly flow at low qualities and stratified flows at higher qualities.

### 3.2.2. Impact of flow-regime on pressure drop and heat transfer

Flow visualization is a key aspect of understanding both the pressure drop and heat transfer characteristics of two-phase

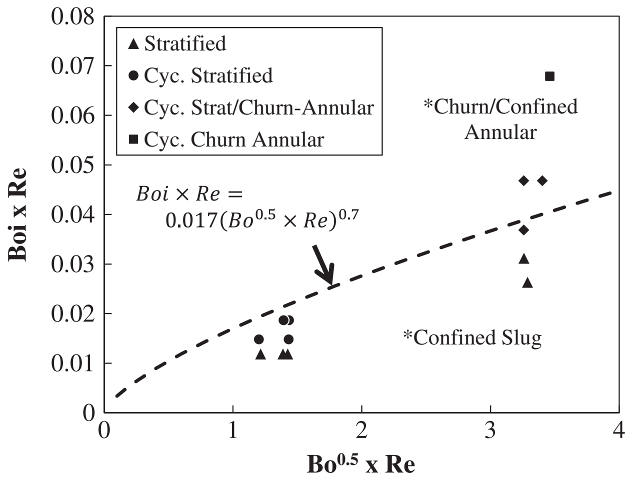


**Fig. 13.** Flow map and transition criteria as proposed by Harirchian and Garimella (2010). Their reported flow regimes is included (*) for comparison. The curve indicates when slug type flows become churn/annular in nature. The transition criteria developed predicts the churn type flows seen in our device quite well, but the predicted slug type flows are manifested as stratified flow in our device due to the hydrophobicity of the membrane.

devices. We first consider the difference in the flow regime and pressure drop between the adiabatic and diabatic experiments presented in this work. Fig. 12 shows that at a mass flux of 140 kg/s/m$^2$ and quality >4% the adiabatic flows are smooth stratified but the diabatic flows are cyclical stratified. Liquid film thinning and periodic dryout, features of the cyclical stratified flow, would alter the heat transfer from what would have been predicted from the smooth stratified films observed during adiabatic flow at the same quality. A comparison of the viscosity scaled two-phase pressure drop finds the diabatic pressure drop to be higher by an average of about 8 kPa at the lower mass flux and lower by about 6 kPa at the higher mass flux of 340 kg/s/m$^2$. Due to the small number of comparative data points in the current study, firm conclusions on the nature of this pressure drop difference is currently not available and is a key area for further study.

The current work can also help explain some of the characteristics of multi parallel-channel vapor venting heat exchangers (David et al., accepted for publication). In that study we fabricated and tested a vapor venting copper heat exchanger with nineteen approximately square channels of hydraulic diameter 133 µm. We found that at a low mass flux of 102 kg/s/m$^2$ the pressure drop could be well predicted by a correlation based vapor venting two-phase model but as the mass flux was increased up to 420 kg/s/m$^2$, the model increasingly under-predicted the pressure drop improvement. In experiments carried out with a non-venting device with one of the walls replaced with the hydrophobic membrane, we found an unexpected improvement in pressure drop at a mass-flux of 420 kg/s/m$^2$ but not at 102 kg/s/m$^2$. From a thermal standpoint, we found that the two-phase heat transfer coefficient in the venting device at the lowest mass flux was lower than predicted using the two-phase heat transfer correlations that was developed from non-venting two-phase flow and even lower than the non-venting control (no membrane) two phase heat exchanger. A similar finding was observed in the non-venting, membrane integrated device. However, the heat transfer coefficient improved at the three higher tested mass fluxes and was comparable or higher than the non-venting control.

These experimental observations can be explained by the flow regimes observed here. At the lower mass flux of 140 kg/s/m$^2$, the flow regime is generally dominated by well behaved stratified flow but at the higher mass flux of 340 kg/s/m$^2$ becomes more chaotic and annular in nature. Simulations of stratified and annular flow find that there is not a significant difference in the pressure drop for either case, thus explaining the agreement between the modeled and measured normalized pressure drop at low mass flux. However, at the higher mass flux, the deposition of liquid droplets on the non-wetting hydrophobic membrane surface during annular film breakup helps reduce the pressure drop beyond that captured by separated flow models since these droplets can more easily be removed by sliding along the hydrophobic membrane. Formation of these liquid drops that flow through the channel without significantly participating in phase change might result in earlier dry-out as compared to a traditional two-phase heat exchanger. Further work is necessary to confirm if this is indeed the case. For the thermal observations, if we assume that the two-phase heat transfer coefficient is dominated by thin film evaporation, stratified flow with a single thick liquid film is thermally inferior to annular type flows with thin liquid films on all the walls. Thus stratified-type flow would result in the poorer than expected heat transfer coefficients observed at the lower mass flux. As mass fluxes increase the formation of churn annular type flows in the venting device results in improved heat transfer coefficients similar to what would be expected from a traditional two-phase heat exchanger experiencing a similar flow regime.

The hydraulic and thermal results obtained from the multi-microchannel heat exchanger study and the differences in the pressure drop and transient behavior of the flow regime between adiabatic and diabatic operation of the current single channel device, highlights the need for diabatic flow regime studies to properly design and analyze the hydraulic and thermal performance of vapor venting microfluidic heat exchangers.

## 4. Design guidelines for venting devices

From the findings in this paper we can make the following general recommendations for a gas/vapor venting device:

(i) Increasing the total membrane-channel contact area increases the maximum quality a channel can support before maximizing its venting effectiveness.
(ii) Increasing the trans-membrane pressure by addition of an outlet choke or a vacuum to the vent side of the membrane also increases the maximum flow quality a channel can support before maximizing its venting effectiveness.
(iii) Gas and vapor venting effectiveness is fundamentally limited by the membrane permeance which increases with membrane permeability and reduces with thickness. Thin, thermally and mechanically stable membranes, with high permeability are ideal.
(iv) Gas venting from devices can be improved by reducing the flow velocity allowing the gas bubbles that form sufficient time to fill the channel and attach to the membrane before transitioning to form less desirable annular type venting flow structures.
(v) In vapor venting heat exchangers, unlike in gas-venting devices, churn-annular type flows that are dominant at higher mass fluxes during phase change offer improved heat transfer coefficients and pressure drop versus stratified type flows that are more prevalent at lower mass fluxes. Thus, for diabatic vapor venting heat exchangers higher liquid velocities may be preferable.

Heat transfer and pressure drop results and correlations, for vapor venting two-phase flow during flow boiling in microchannels, have been documented in the work by David et al. (accepted for publication), and are not presented here due to the relatively small number of diabatic data points.

## 5. Conclusion

In the work presented in this paper we have developed and tested a single microchannel copper device that allows visualization of venting flow structures through a porous hydrophobic Teflon membrane and porous carbon-mesh membrane. Phase separation and removal through the membranes was studied both adiabatically and diabatically by injecting air through a T-junction and by heating until vaporization respectively. Mass qualities of 0.1–7% were achieved in the adiabatic experiments and up to 20% during diabatic experiments. The flow regimes obtained in each was visualized, mapped and compared to key work in the field highlighting the differences in observed flow structures when a hydrophobic membrane is incorporated.

Adiabatically we find bubbly flows at low qualities, changing to wavy stratified and smooth stratified as air injection rates increase. At higher liquid flow-rates the behavior changes resulting in 'jetting' type breakup and the formation of annular type flows that are not conducive to air venting. During diabatic operation we find bubbly and slug type flows at low qualities followed by stratified and cyclical stratified flows at higher qualities and low liquid flow rates. As the flow rate is increased we instead see churn-annular type flows forming at higher qualities. The occurrence of churn-annular type flows is believed to help improve heat transfer coefficients and two-phase pressure drops.

Analysis of the venting rates during adiabatic operation finds that the maximum quality the device can support before maximizing its venting effectiveness can be improved by adding an outlet choke, reducing vent-side pressure, increasing the membrane-channel area and using thin membranes with higher permeabilities. We also find that venting effectiveness does not depend on the Weber number as long as the air-structures interact with the membrane.

This work represents an important step in the design of a gas and vapor venting devices, particularly vapor venting heat exchangers, by generating a preliminary flow-regime map for a phase separated two-phase flows and experimentally identifying several factors that help improve venting effectiveness. The work also highlights the importance of flow regime in explaining measured heat transfer and pressure drops in bulk vapor-venting heat exchangers. Improved vapor venting is key to overcoming instability issues and increased pressures that currently hinder the implementation of two-phase microfluidic heat exchangers.

## Acknowledgements

The authors would like to acknowledge the support of the MARCO Interconnect Focus Center, one of five research centers funded under the Focus Center Research Program, a Semiconductor Research Corporation (SRC) program. The author also appreciates support from the SRC as well as the Stanford Graduate Fellowships. The authors also thank the Stanford TSD Machine-shop for fabricating the copper samples.

## References


2009 ITRS [WWW Document], 2011. URL <http://www.itrs.net/Links/2009ITRS/Home2009.htm>.

Alexander, B., Wang, E., 2009. Design of a microbreather for two-phase microchannel heat sinks. Nanoscale Microscale Thermophys. Eng. 13, 151–164.

Bernstein, K., Puri, R., Young, A., Andry, P., Cann, J., Emma, P., Greenberg, D., Haensch, W., Ignatowski, M., Koester, S., Magerlein, J., 2007. Interconnects in the third dimension. In: Proceedings of the 44th Annual Conference on Design Automation – DAC '07. San Diego, California, 562-56.

Carey, V., 1992. Introduction to two-phase flow. In: Liquid–Vapor Phase-Change Phenomena: An Introduction to the Thermophysics of Vaporization and Condensation Processes in Heat Transfer Equipment. Hemisphere Pub. Corp., Washington DC, pp. 399–452 (Chapter 10).

Cheng, L., Ribatski, G., Thome, J.R., 2008. Two-phase flow patterns and flow-pattern maps: fundamentals and applications. Appl. Mech. Rev. 61, 050802.1–050802.28.

Chung, P., Kawaji, M., 2004. The effect of channel diameter on adiabatic two-phase flow characteristics in microchannels. Int. J. Multiph. Flow 30, 735–761.

Cubaud, T., Ho, C.-M., 2004. Transport of bubbles in square microchannels. Phys. Fluids 16, 4575–4585.

David, M.P., Khurana, T., Hidrovo, C., Pruitt, B.L., Goodson, K.E., 2007. Vapor-venting, micromachined heat exchanger for electronics cooling. In: Heat Transfer, Fluid Flows, and Thermal Systems, Parts A and B – ASME 2007 IMECE, vol. 8. Seattle, Washington, USA, pp. 951–960.

David, M.P., Marconnet, A.M., Goodson, K.E., 2008. Hydrodynamic and thermal performance of a vapor-venting microchannel copper heat exchanger. In: Sixth International ASME Conference on Nanochannels, Microchannels and Minichannels – ICNMM 2008. Darmstadt, Germany, pp. ICNMM2008-62269.

David, M.P., Miler, J., Steinbrenner, J.E., Touzelbaev, M., Yang, Y., Goodson, K.E., accepted for publication. Hydraulic and thermal characteristics of a vapor venting microchannel heat exchanger. Int. J. Heat Mass Transfer.

De Menech, M., Garstecki, P., Jousse, F., Stone, H.A., 2008. Transition from squeezing to dripping in a microfluidic T-shaped junction. J. Fluid Mech. 595, 141–161.

Fang, C., David, M., Rogacs, A., Goodson, K., 2010. Volume of fluid simulation of boiling two-phase flow in a vapor-venting microchannel. Front. Heat Mass Transfer 1.

García-Payo, M., Izquierdo-Gil, M.A., Fernandez-Pineda, C., 2000. Wetting study of hydrophobic membranes via liquid entry pressure measurements with aqueous alcohol solutions. J. Colloid Interf. Sci. 230, 420–431.

Garimella, S., Singhal, V., 2004. Single-phase flow and heat transport and pumping considerations in microchannel heat sinks. Heat Transfer Eng. 25, 15–25.

Garstecki, P., Fuerstman, M.J., Stone, H.A., Whitesides, G.M., 2006. Formation of droplets and bubbles in a microfluidic T-junction—scaling and mechanism of break-up. Lab Chip 6, 437–446.

Harirchian, T., Garimella, S.V., 2009. Effects of channel dimension, heat flux, and mass flux on flow boiling regimes in microchannels. Int. J. Multiph. Flow 35, 349–362.

Harirchian, T., Garimella, S.V., 2010. A comprehensive flow regime map for microchannel flow boiling with quantitative transition criteria. Int. J. Heat Mass Transfer 53, 2694–2702.

Hetsroni, G., Mosyak, A., Segel, Z., Ziskind, G., 2002. A uniform temperature heat sink for cooling of electronic devices. Int. J. Heat Mass Transfer 45, 3275–3286.

Hetsroni, G., Mosyak, A., Pogrebnyak, E., Segal, Z., 2005. Explosive boiling of water in parallel micro-channels. Int. J. Multiph. Flow 31, 371–392.

ITRS Update [WWW Document], 2011. URL <http://www.itrs.net/Links/2010ITRS/Home2010.htm>.

Jiang, L., Wong, M., 2001. Forced convection boiling in a microchannel heat sink. J. Microelectromech. Syst. 10, 80–88.

Kandlikar, S.G., 2004. Heat transfer mechanisms during flow boiling in microchannels. J. Heat Transfer 126, 8–16.

Kandlikar, S., Grande, W., 2004. Evaluation of single phase flow in microchannels for high heat flux chip cooling – thermohydraulic performance enhancement and fabrication technology. Heat Transfer Eng. 25, 5–16.

Kandlikar, S., Shoji, M., Dhir, V.K., 1999. Handbook of Phase Change: Boiling and Condensation. Taylor & Francis, Philadelphia, PA.

Kays, W., Crawford, M.E., 1993. Convective Heat and Mass Transfer, third ed. McGraw-Hill, New York.

Koo, J.-M., Im, S., Jiang, L., Goodson, K.E., 2005. Integrated microchannel cooling for three-dimensional electronic circuit architectures. J. Heat Transfer 127, 49–58.

Lee, P., Garimella, S., 2008. Saturated flow boiling heat transfer and pressure drop in silicon microchannel arrays. Int. J. Heat Mass Transfer 51, 789–806.

Marconnet, A.M., David, M.P., Rogacs, A., Flynn, R.D., Goodson, K.E., 2008. Temperature-dependent permeability of microporous membranes for vapor venting heat exchangers. In: Heat Transfer, Fluid Flows, and Thermal Systems, Parts A, B, and C – ASME 2008 IMECE, vol. 10. Boston, Massachusetts, USA, pp. 1005–1012.

Meng, D.D., Cubaud, T., Ho, C.-M., Kim, C.-J., 2007. A methanol-tolerant gas-venting microchannel for a microdirect methanol fuel cell. J. Microelectromech. Syst. 16, 1403–1410.

Pasaogullari, U., Mukherjee, P.P., Wang, C.-Y., Chen, K.S., 2007. Anisotropic heat and water transport in a PEFC cathode gas diffusion layer. J. Electrochem. Soc. 154, B823–B834.

Qu, W., Mudawar, I., 2002. Experimental and numerical study of pressure drop and heat transfer in a single-phase micro-channel heat sink. Int. J. Heat Mass Transfer 45, 2549–2565.

Qu, W., Mudawar, I., 2003. Measurement and prediction of pressure drop in two-phase micro-channel heat sinks. Int. J. Heat Mass Transfer 46, 2737–2753.

Revellin, R., Thome, J.R., 2007. A new type of diabatic flow pattern map for boiling heat transfer in microchannels. J. Micromech. Microeng. 17, 788–796.

Sinha, P.K., Mukherjee, P.P., Wang, C.-Y., 2007. Impact of GDL structure and wettability on water management in polymer electrolyte fuel cells. J. Mater. Chem. 17, 3089–3103.

Steinke, M.E., Kandlikar, S.G., 2004. An experimental investigation of flow boiling characteristics of water in parallel microchannels. J. Heat Transfer 126, 518–526.

Taitel, Y., Dukler, A.E., 1976. A model for predicting flow regime transitions in horizontal and near horizontal gas–liquid flow. AIChE J. 22, 47–55.

Thome, J., Dupont, V., Jacobi, A.M., 2004. Heat transfer model for evaporation in microchannels. Part I: presentation of the model. Int. J. Heat Mass Transfer 47, 3375–3385.

Tong, L.S., Tang, Y.S., 1997a. Boiling heat transfer and two-phase flow, second ed. Taylor & Francis, Washington, DC.

Tong, L.S., Tang, Y.S., 1997b. Instability of two-phase flow. In: Boiling Heat Transfer and Two-phase Flow. Taylor & Francis, Washington, DC, pp. 457–480 (Chapter 6).

White, F.M., 1991. Solutions of the Newtonian viscous flow equations. In: Viscous Fluid Flow, Mechanical Engineering. McGraw-Hill, Boston, Massachusetts, pp. 104–217 (Chapter 3).

Wu, H., Cheng, P., 2004. Boiling instability in parallel silicon microchannels at different heat flux. Int. J. Heat Mass Transfer 47, 3631–3641.

Zhang, L., Koo, J.-M., Jiang, L., Asheghi, M., Goodson, K.E., Santiago, J.G., Kenny, T.W., 2002. Measurements and modeling of two-phase flow in microchannels with nearly constant heat flux boundary conditions. J. Microelectromech. Syst. 11, 12–19.

Zhang, T., Tong, T., Chang, J.-Y., Peles, Y., Prasher, R., Jensen, M.K., Wen, J.T., Phelan, P., 2009. Ledinegg instability in microchannels. Int. J. Heat Mass Transfer 52, 5661–5674.